Data Fusion for Increasing Monitoring Capabilities of Sentinel Optical Data in Marine Environment

Maria Kremezi ⬡ and Vassilia Karathanassi

Abstract—Marine monitoring constitutes one of the main thematic areas of the Sentinel mission. The Sentinel 3 OLCI (S3) sensor provides satellite data for services relevant to the ocean and land. While the spatial resolution of S3 images (300 m) is suitable for most marine applications, there are some applications such as floating debris detection, suspended mater estimation, etc., that require higher resolution. To fulfill this requirement this study applies an unmixing-based data fusion technique on S3 and BRDF-corrected Sentinel 2 (S2) images and evaluates the fused data by calculating the correlation coefficient and the spectral angle distance (SAD) indexes. Then, it explores the increased monitoring capabilities of the fused image by applying improved chlorophyll-a (Chl-a) and total suspended matter (TSM) algorithms, developed for satellite data. The fused image presents spectral similarity to S3 data and spatial similarity to S2 image. Consequently, the products provided by the fused image have much better resolution than those of S3 image, which enables detailed estimations of Chl-a and TSM concentrations. However, the dynamic nature of the marine environment that results in the formation of time-varying patterns at sea surface, in relation to the time lag between S2 and S3 image acquisitions may locally affect the accuracy of the products in the neighborhood of these patterns. This study exploits the effective elimination of directional reflectance effects in S2 ocean images, interprets the fused image and the generated ocean products, and points out the constraints regarding the synergy of Sentinel optical data for ocean areas.

Index Terms—Bidirectional reflectance distribution function (BRDF) correction, chlorophyll-a (Chl-a), data fusion, marine monitoring, sentinel, spectral unmixing, total suspended matter (TSM).

I. Introduction

SENTINEL 3 OLCI products aim at supporting 1) marine safety, where the quality of the ocean is observed, 2) marine resources, where resources in the marine environment are detected and studied, 3) marine and coastal environment, where it is observed how these environments are affected by natural processes or human intervention, and 4) sea ice, where the behavior of frozen ocean water is examined. The 300 m spatial resolution matches most of the requirements for the above applications. However, there are cases, such as floating debris

detection, coastal suspended mater estimation, small-scale upwelling etc., where data with higher resolution are required. Fusion of Sentinel 2 and Sentinel 3 images can address this issue for coastal ocean areas, and the Mediterranean Sea, for which data from both missions are available. Two challenges need to be addressed. The first is the significant bidirectional reflectance distribution function (BRDF) effects over water bodies depicted in Sentinel 2 data, whereas the second is related to the dynamic nature of the marine environment. To face the first, the authors in previous works applied the kernel-based BRDF model, which yielded satisfactory results [1], and compared the model with other state-of-the-art methods proving its superiority [2]. To face the second, thorough interpretation of the fusion results is required. The main goal of effective data fusion methods is to preserve the spatial and spectral information presented in the high spatial and high spectral resolution images, respectively, when merging the data. But, unlike landforms and manmade objects, the spatial characteristics of sea water present serious variations in time, making the interpretation of the fused image a hard task, when the two images are acquired at different time. Previous work regarding fusion of ocean images was implemented for the panchromatic and multispectral bands of Landsat 8 imagery focusing on improving the spatial resolution of total suspended matter (TSM) maps [3]. In this study, ocean S2 and S3 images were fused and chl-a and TSM maps were produced. The fused image has been evaluated using two metrics, and its enhanced marine monitoring capabilities were explored through the application of improved Chl-a and TSM algorithms, developed for ocean satellite data. This article, apart from evaluating the synergy of Sentinel 2 and 3 images, raises concerns that aim at increasing our understanding about the fusion result of ocean images and the derived ocean products.

II. Related Work

Image fusion techniques emerged from multispectral (MS) pansharpening techniques, where MS images are fused with a panchromatic band (PAN) in order to improve their spatial resolution. A variety of image fusion techniques has been developed, which can be roughly classified into seven categories: component substitution (CS), multiresolution analysis (MRA) [4], hybrid [5], Bayesian [6], unmixing-based [7]–[16], tensor-based [17], and deep learning methods [18].

The unmixing-based methods rely on the spectral unmixing theory and exploit all the bands of the common spectral region of the initial images, which is an advantage when images with many

bands have to be fused. Although the numerous narrow bands acquired by a hyperspectral sensor (HS) are the ideal dataset for applying spectral unmixing models, these models have been also proved useful tools for decomposing the mixed pixels of MS datasets. According to unmixing-based fusion methods, the high spatial resolution image is a spectrally degraded form of the high spectral resolution image and vice versa, the high spectral resolution image is a spatially degraded form of the high spatial resolution image. In [7] and [8], the unmixing process was implemented sequentially on the HS and MS images resulting in endmembers extracted from the HS image and abundance matrices from the MS image by using the spectrally transformed HS endmembers. The fusion result is the multiplication of the HS endmembers with the MS abundance matrices. Yokoya *et al.* [9] used the spatial spread and spectral response transform matrices that relate the two datasets and alternately applied the non-negative matrix factorization method on the two datasets until convergence. The obtained high spectral resolution endmember and high spatial resolution abundance matrices were used for the construction of the fused image. Lanaras *et al.* [10] suggested a projected gradient method into the alternate updates of the endmember and abundances matrices for reaching convergence. Akhtar *et al.* [11] using the Bayesian dictionary learning, learned distributions for the scene spectra and their proportions in the image. This information has been used to sparse code the high spatial resolution image. Nezhad *et al.* [12] formulated the fused image reconstruction problem as an ill-posed linear inverse problem, since the number of MS bands is usually lesser than the number of endmembers. Thus, they included a regularization term to convert it into a well-posed inverse problem. The regularization term was constructed based on spectral coding (SC). For SC, a dictionary based on several high spatial resolution MS or PAN images has been used. Simões *et al.* [13] included an abundance regularization to achieve spatial smoothness of the abundances and ensure that the fused image retains both the spatial and spectral correlation, whereas Luo *et al.* [14] proposed the adversarial selection fusion (ASF) method. After a conventional unmixing-based fusion and a preliminary fused image reconstruction by the optimized band image dictionary and reconstruction coefficients, a spectral-spatial quality index was used for guiding the adversarial selection process. Lanaras *et al.* [15] used efficient proximal mappings to impose the constraints, while Wei *et al.* [16] employed an alternating optimization of fusion and unmixing with Sylvester equation solvers.

Most of the aforementioned works use dictionaries and sparse coding. Unfortunately, the lack of spectral libraries for sea water sets severe constraints in their use. In this study, a methodology similar to [7] and [8] has been applied because it is straightforward, requires short processing time and renders the interpretation of the fused image easier. The novelty of this article does not lie on the development of new data fusion algorithms, but rather 1) on the attempt to use an unmixing-based fusion process on S2 and S3 images for producing higher resolution ocean map products (e.g., Chl-a and TSM), and 2) on the investigation of the suitability of such a technique for dynamically changing environments (i.e., oceans).

III. UNMIXING-BASED DATA FUSION METHOD

Given a hyperspectral image $H \in \mathbb{R}^{k \times n \times B}$ with high spectral resolution (B number of bands) and low spatial resolution ($k \times n$ number of pixels) and a MS image $M \in \mathbb{R}^{K \times N \times b}$ with high spatial resolution ($K \times N$ number of bands, where $K \times N >> k \times n$) and low spectral resolution (b number of bands, where $b << B$), the fusion method aims to combine information from both images to a single image $F \in \mathbb{R}^{K \times N \times B}$ with high spectral and spatial resolution.

According to linear mixing model (LMM), each pixel is a linear combination of numerous independent signals and spectral unmixing aims to analyze the composition of these mixed pixels into their endmembers and their corresponding abundances. In this case, the spectrum of a mixed pixel (f) is a linear combination of the endmember spectra weighted by the fractional area coverage of each endmember in a pixel.

$$f_{i,j} = \sum_{z=1}^{p} e_z a_z + u_{i,j} \tag{1}$$

where $e_z \in \mathbb{R}^B$ is the spectral signature (reflectance) of the $z \in \{1, \ldots, p\}$ endmember, a_z is its corresponding abundance, p is the number of endmembers (pure pixels) and $u_{i,j}$ is the remaining error. Two constraints are usually posed on the LMM model: the nonnegativity (abundance and endmember values must be positive numbers) and the sum-to-one constraint (the sum of the abundance values must equal to one). In case that both constraints are posed, the fully constrained LMM (FC-LMM) is applied. In matrix form the fused image can be described as follows [15]:

$$F = EA \tag{2}$$

where $E \equiv [e_1, e_2, \ldots, e_p] \in \mathbb{R}^{B \times p}$ is the matrix of all the endmembers present in the image and $A \equiv [a_1, a_2, \ldots, a_{(K \times N)}] \in \mathbb{R}^{p \times (K \times N)}$ is the matrix of abundances of each endmember for every pixel of the fused image. The abundances can be estimated by unconstrained, nonnegativity constrained, and fully constrained least squares unmixing.

Furthermore, the hyperspectral image H with low spatial resolution can be expressed as a spatially downsampled F

$$H \approx FS = EAS \tag{3}$$

where $S \in \mathbb{R}^{(K \times N) \times (K \times N)}$ is the downsampling operator in the spatial dimension and it can be a simple average filter. While the MS image M can be expressed as a spectrally downsampled F

$$M \approx RF = REA \tag{4}$$

where $R \in \mathbb{R}^{b \times B}$ is the spectral response function (SRF) of the MS sensor and it is provided by the sensor manufacturer.

An estimation of A and E can be achieved through optimization techniques that use iterations. Though, based on the studies in [8] and [19] endmembers can be extracted from the hyperspectral image and then spectrally downsampled to the resolution of the MS image. Then, the LMM is applied on M and matrix A is estimated through least squares.

The rich spectral resolution of HS imagery in contrast to the lower of MS allows the accurate detection of endmembers.
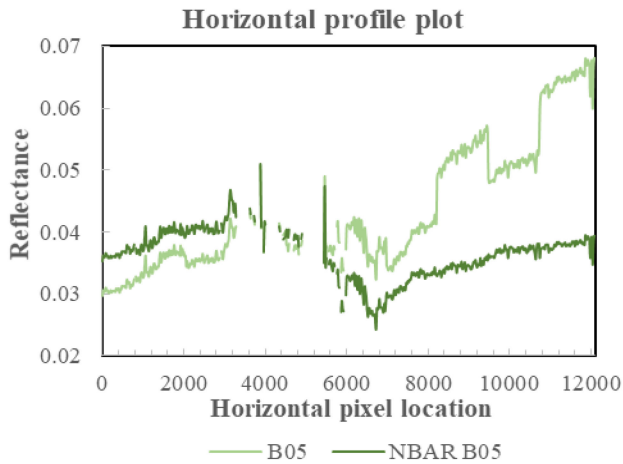
Horizontal profile plot

Fig. 1. Horizontal profile (line 10 000) from the original S2 and the NBAR mosaic for band B05 (704.1 nm). The profile includes the detectors from 3 to 12.

Several endmember extraction approaches require the number of endmembers to be known *a priori*. The dimension of the signal subspace is used to determine the number of the endmembers. In this study, the outlier detection method (ODM) [20] was utilized for signal subspace estimation and the N-FINDR method [21] for extracting the endmembers.

ODM is an automatic nonparametric method for estimating the number of endmembers, which considers only the existence of noise and treats signals as outliers of noise [20]. N-FINDR is based on the assumption that pure pixel endmembers exist in the image.

IV. IMPLEMENTATION

A. Datasets

The study area is part of the Ionian Sea, Southwest of Greece. The MS dataset consists of eight Sentinel 2 (S2) MSI Level 1C satellite images (granules) captured on August 27, 2017. The 13 spectral bands have 10, 20, or 60 m spatial resolution and cover the spectral range 0.4–2.2 μm. The images were resampled at 20 m spatial resolution and merged into a mosaic image. The resulting image has a spatial size of 15 500 $\times$ 15 500 pixels and 13 bands. Bands 1–5 and 7–9 (0.4–0.9 μm) were used in the fusion process as for these bands, SRF measurements are available. The S3 OLCI level 1 dataset consists of one image captured the same day but less than an hour before S2 data capture. This becomes clear by comparing the location of the ships in Fig 1(c) and (d). The OLCI measures reflected solar radiation in 21 spectral bands in the range 0.4–1.0 μm and the full spatial resolution is around 300 m resulting in an image with 760 $\times$ 1030 pixels. In this study, S3 dataset is considered as the hyperspectral dataset.

B. Preprocessing

After resampling the S2 dataset, the cloud masking process was implemented. It is very important because clouds and their shadows can be confused with sun glint water areas and water,

respectively. The Fmask (Function of mask) cloud masking algorithm [22] was applied. The algorithm computes cloud probabilities by applying thresholds on the optical and the cirrus band in order to determine if a pixel is water, land, cloud, cloud shadow or snow. In this study, the cloud probability threshold was set to 10% and the cloud and cloud shadow dilation was set to 5 pixels. For the S3 dataset, the cloud masking procedure was carried out manually with attention to mask out all cloud and shadow pixels as well as all land by extending the shoreline a bit. Both datasets were converted to top-of-atmosphere reflectance and atmospheric corrections were not applied.

C. BRDF Correction

The MSI features two distinct arrays of 12 detectors mounted on two focal planes. The 12 detectors on each focal plane are in a staggered configuration with different view azimuth angles each. The difference in azimuth angles between neighboring detectors vary from 25° to 100° resulting in significant directional reflectance effects over non-Lambertian surfaces, which are described by the BRDF. These effects may be trivial over land surface but they are very significant over water bodies due to their optical properties. This dataset needs to be calibrated prior to the fusion application. For this, calibration the kernel-based model was exploited as it is used to simulate the BRDF [1]. The BRDF is expressed as a linear sum of kernels. This model was developed by Roujean *et al.* [23]

$$R\left(\theta, \vartheta, \phi, \lambda\right) = f_{\text{iso}} + f_{\text{vol}} K_{\text{vol}} + f_{\text{geo}} K_{\text{geo}} \qquad (5)$$

where R is the estimated reflectance in wavelength λ, K_{vol}, K_{geo} are the volumetric scattering (Ross–Thick) and geometric (Li-Sparse) kernels of the model that depend on the viewing geometry of the sensor and the sun. The kernels are based on the radiative transfer theory and are expressed as a function of the solar zenith angle (θ), the view zenith angle of the sensor (ϑ) and the relative azimuth angle (φ) [23], [24]. The f parameters are calculated by inverting the BRDF model and through the least square approach using the S2 data.

The BRDF model is then used to adjust the observed reflectance to nadir viewing. The Nadir BRDF adjusted reflectance (NBAR) is calculated by multiplying the observed reflectance by the c factor. The c factor is defined by the ratio of reflectance calculated using the kernel-based BRDF model for a fixed nadir geometry and the observed geometry.

$$\text{NBAR}\left(\theta, 0, \lambda, \varphi\right) = c\left(\theta, \vartheta, \lambda, \varphi\right) R_{\text{observed}} \qquad (6)$$

$$c\left(\theta, \vartheta, \lambda, \varphi\right) = \frac{R\left(\theta, 0, \phi, \lambda\right)}{R\left(\theta, \vartheta, \phi, \lambda\right)} \qquad (7)$$

where R is the reflectance calculated by the BRDF model for zero view zenith angle of the sensor in the nominator and the specific angle with which each is pixel is viewed by the sensor in the dominator. NBAR takes into account the viewing and sun geometry, so the correction of directional reflectance effects is carried out for both azimuth and zenith angle differences. In Fig. 1, a horizontal profile plot from band B05 (704.1 nm) of the original S2 mosaic image as well as the NBAR of the same band
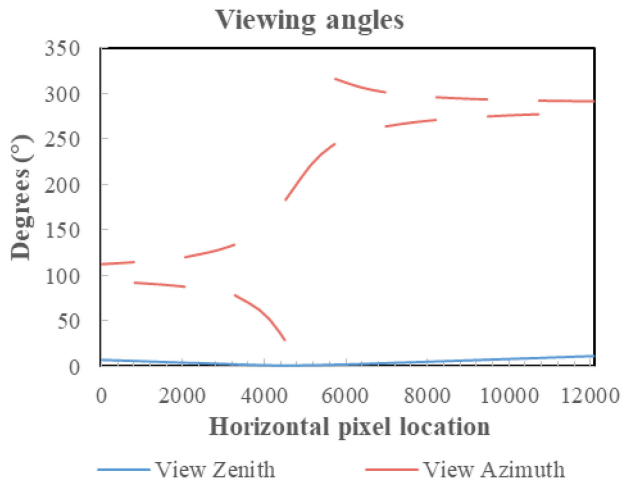
Fig. 2.   Horizontal profile (line 10 000) of the viewing geometry for the S2 mosaic for band B05 (704.1 nm). The profile includes the detectors from 3 to 12.

are shown. Moreover, in Fig. 2, the view angles for the same horizontal profile are presented.

The processing lasts approximately 20 min for each one of the spectral bands, using a computer with Intel Core i7-8850U 1.80 GHz 1.99 GHz and 16 GB RAM. It is important to point out the vast size of the dataset. Heuristic tricks (like sampling one pixel every 20 rows × 20 columns) and parallel processing could significantly improve the processing time.

D. Data Fusion

The endmember extraction algorithm when applied on the S3 dataset yielded five endmembers, which in turn were spectrally transformed to fit Sentinel 2 spectra according to the SRF of the S2 sensor provided by ESA. Then, the FC-LMM was applied on S2 image to compute the abundance maps. Afterward, the fusion image was constructed by using the above abundance maps and S3 spectra. In Fig. 3, the S2 image before and after the BRDF correction, the S3 image, as well as the fusion result of a part of the study area is displayed. The unmixing and reconstruction procedures were implemented in the aforementioned computer system and totally lasted approximately 30 min. However, parallel programming could significantly reduce the computation time.

V. Evaluation

From visual interpretation, the significant BRDF effects on sea water caused by the configuration of S2 detectors can be observed. The corrected S2 image does not depict observable reflectance variations, whereas the morphology of sea surface is kept with the majority of sea surface patterns being observable [1]. In the lower spatial resolution (300 m) of S3 image, the sea water appears smoother presenting reduced features on the sea surface. The fused image presents similar morphology to S2 image (see Fig. 3). It is observed that the fused image keeps the spatial characteristics of S2 image. This is expected since the
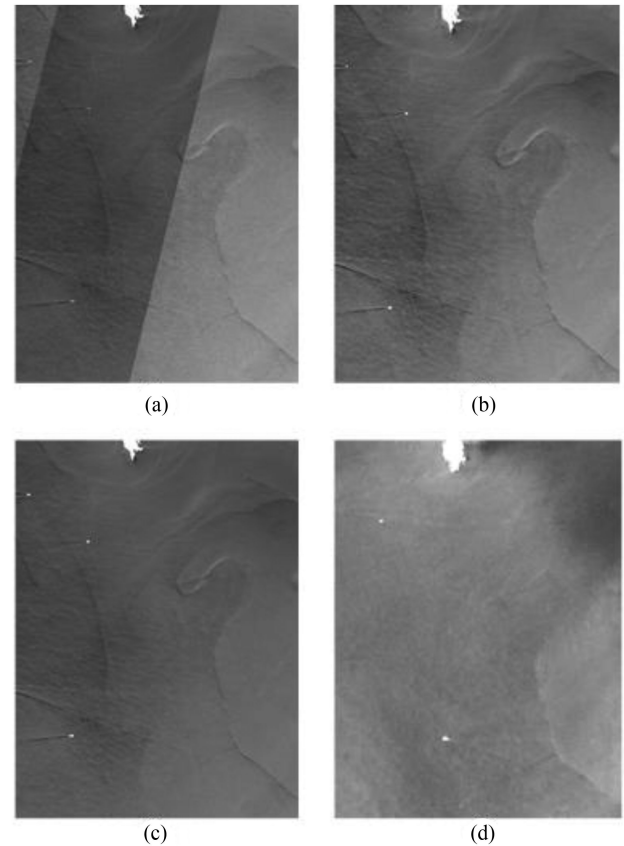

Fig. 3.   Part of the study area: (a) Sentinel 2—band 5 (704.1 nm) before BRDF correction, (b) Sentinel 2—band 5 (704.1 nm) after BRDF correction (c) Fused image—band 11 (708.75 nm), and (d) Sentinel 3—band 11 (708.75 nm).

abundance maps used to produce the fused image are estimated by using the S2 image. Because the spatial characteristics of sea water are dynamic and change through time, the fused image seems to be more similar to S2 image, although the used spectra (endmembers) are those resulting from S3 image.

For the quality assessment of the fused image the correlation coefficient (CC) and spectral angle distance (SAD) indices [25] have been used. The CC is a statistical measure of the strength of the relationship between the relative movements of two variables. The extreme values of -1 and 1 indicate a perfectly linear relationship where a change in one variable is accompanied by a perfectly consistent change in the other. A coefficient of zero represents nonlinear relationship. As one variable increases, there is no tendency in the other variable to either increase or decrease.

In Fig. 4, the values of the CC index between the fused and S2 image (green line) and the fused and S3 image (red line) are displayed.

For the comparison between the fused and S2 image, the CC was calculated between bands with close wavelengths and 20 m spatial resolution. For the comparison between the fused and S3 image, the CC was calculated between all bands, after resampling the fused image to 300 m spatial resolution. Values very close to 1 are observed for the fused and S2 image. This is not the case for the correlation between the fused and S3 image,
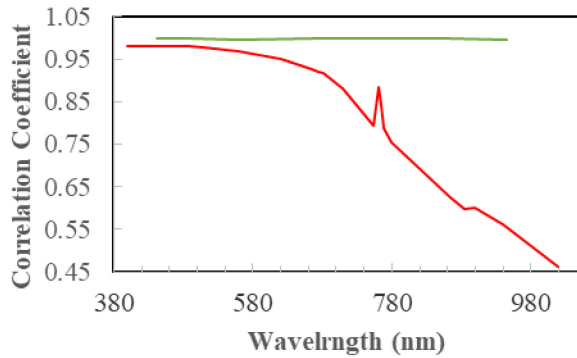
Fig. 4. CC Index for the fused image and S2 image (green) and for the fused image and S3 image (red).

(a)   (b)

Fig. 5. Chlorophyll-a concentration maps for a representative part of the (a) fused image, (b) Sentinel 3 image.

TABLE I
SPECTRAL ANGLE DISTANCE

SAD value	Fused - S3	Fused - S2
	% of the whole image	
0	17.36	17.30
(0 , 0.1]	74.81	0.03
(0.1 , 0.2]	7.47	0.05
(0.2 , 0.3]	0.06	82.30
(0.3 , 0.4]	0.04	0.03
(0.4 , 0.5]	0.04	0.05
(0.5 , 0.6]	0.06	0.07
(0.6 , 0.7]	0.06	0.08
(0.7 , 0.8]	0.05	0.06
(0.8 , 0.9]	0.04	0.03
(0.9 , 1]	0.00	0.00

as the index is close to 0.95 for the VIS part of spectrum and it decreases to 0.5 for the NIR part of the spectrum.

The SAD indicates how similar the spectral signatures of two pixels are. The SAD index is not affected by illumination conditions. A SAD value of zero represents identical spectral signatures, while values close to 1.58 rad show very different (orthogonal) spectral signatures. For the spectral comparison of the fused image to its constituents, the fused image was 1) resampled to 300 m pixel resolution in order to calculate SAD with S3 image, and 2) spectrally transformed by the SRF of the S2 sensor, in order to calculate SAD with S2 image. The SAD (see Table I) shows very high spectral similarity between the fused and Sentinel 3 image with approximately 92% of the pixels having less than 0.1 distance. Lower percentages can be observed for the spectral similarity between the fused and Sentinel 2 image as for around 80% of the pixels, the SAD values range from 0.2 to 0.3 and only for the 17% of the pixels, the value is 0. This was again expected because the fused image is spectrally reconstructed with endmembers extracted from the S3 image.

VI. INCREASING MARINE MONITORING CAPABILITIES OF THE SENTINEL DATA

Retrieval of many ocean products such as Chl-a, TSM, inherent optical properties, CDOM, etc., may be improved by the enhanced spectral and spatial resolution of the fused image. In this study, two algorithms, for Chl-a and TSM estimation, respectively, were appli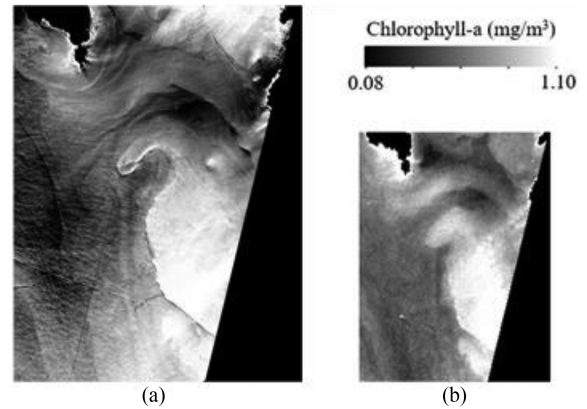ed on the fused image. Both algorithms utilize bands of the S3 sensor that the S2 sensor is not designed to include. These bands are proven to deliver more accurate results for both chl-a [26] and TSM [27], [28] products. The chlorophyll-a product was estimated using the OC6 algorithm, which is proven to be more accurate than other similar algorithms that utilize fewer spectral bands [26]. The OC6 maximum band ratio (MBR) is a semianalytical algorithm and is developed to define the chlorophyll-a concentration. It is a polynomial based on the use of a semianalytical model and analysis of apparent optical properties (AOP's) obtained by *in-situ* measurements in various oceanic regions.

$$\log\left(\text{Chl}\right) = \sum_{x=0}^{3} \left(A_x \left(\log \left(R_j^i \right) \right)^x \right) \qquad (8)$$

where R_j^i is the ratio of reflectance of band i, among 413, 443, 490, 510 nm, over the mean j of bands at 560 and 665 nm. The band for the numerator is selected so that the ratio is maximized.

The algorithm was applied on the S3 and fused images. The resulting chlorophyll-a maps are presented in Fig. 5.

Moreover, the generic multisensor algorithm, transformed to exploit the capabilities of S3 for TSM retrieval in turbid waters was applied [29].

$$\text{TSM} = \frac{A_\rho \pi R_{rs}}{1 - \frac{\pi R_{rs}}{C_\rho}} + B_\rho \qquad (9)$$

where R_{rs} are reflectance values from the 620 nm band, which according to [26], it was proven to provide the least RMSE. The coefficients A_ρ, B_ρ, and C_ρ have been established using *in-situ* measurements [25]. The result of the TSM concentration maps is presented in Fig. 6.

Due to the spectral similarity between the S3 and fused image, the products generated by the fused image are expected to be similar with those of S3 image but with much better resolution. Indeed, the maps provided by the fused image have better resolution than those produced by S3 image. This enables detailed estimations of Chl-a and suspended matter concentrations. However, the patterns on the sea surface that are observed in S2 image are preserved in these products. For example, in the
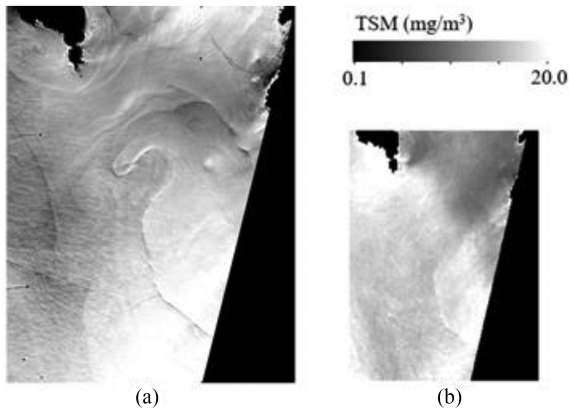
Fig. 6. Total suspended concentration maps for a representative part of the (a) fused image, (b) Sentinel 3 image.

fused image, we observe tails of ships that are observed on the S2 but not on the S3 image. Since such patterns, caused by ships, currents, etc., may locally affect Chl-a concentrations and TSM, false conclusions in relation to the reference time, for Chl-a and TSM estimations may be obtained when using the fused image for the areas that present these patterns. In case of simultaneous capture of S2 and S3 data, effects of ship tails will still be apparent on the ocean products, but will reflect the exact sea state for the data acquisition time. However, further investigation with *in-situ* measurements is needed in order to draw sounder conclusions and perform quantitative analysis of the product accuracy.

VII. CONCLUSION

In this study, the synergy of S2 and S3 data for improving marine monitoring is examined. The driving force of this task was the rising need of high spectral and spatial resolution data for marine monitoring in specific cases, such as coastal suspended mater estimation, small-scale upwelling, floating debris detection, etc. Two challenges have been addressed: the significant BRDF effects on ocean S2 images, and the effects of the dynamic nature of marine environment on data fusion products. The c-factor approach along with the Ross–Li model that simulates the BRDF satisfactorily eliminated bidirectional effects. The fused image produced by the unmixing-based data fusion method is not a spatial enhancement of the S3 image or a spectral enhancement of the S2 image but it contains information of both the original images and is similar to them either spatially or spectrally. The latter in relation to the asynchronous pass of Sentinel satellites affect estimations of Chl-a, turbidity, and other ocean parameters. Even the less than an hour time lag between the pass of S2 and S3 satellites, may cause local inaccuracies in the products of the fused image in the areas, where there are edges from ships, currents, etc., in the S2 image. However, the finer spatial resolution of the fused image and the ability that it gives us to apply improved algorithms for generating ocean products establish the fusion of Sentinel optical data a useful tool for the enhancement of marine research.

Interesting topics for future research are the application of other unmixing-based data fusion algorithms and quantitative evaluation of the ocean products with *in-situ* data measured simultaneously to the pass of the two satellites. The last is very significant for the further analysis of the fused image and the generated ocean products. Furthermore, special interest should be given on the use of the fused data for detecting and monitoring marine pollution.

REFERENCES

[1] M. Kremezi and V. Karathanassi, "Correction of the BRDF effects on Sentinel-2 ocean images," in *Proc. IEEE Int. Geosci. Remote Sens. Symp.*, 2019, pp. 9010–9013.

[2] M. Kremezi and V. Karathanassi, "Correcting the BRDF effects on Sentinel-2 ocean images," in *Proc. 7th Int. Conf. Remote Sens. Geoinform. Environ.*, 2019, Art. no. 111741C.

[3] Q. Vanhellemont and K. Ruddick, "Pan-sharpening to improve spatial resolution of optical remote sensing with examples from Landsat-8 (30m/15m)," in *Proc. Int. Ocean Color Sci. Meeting*, 2015, [Online]. Available: https://www.eposters.net/poster/pan-sharpening-to-improve-spatial-resolution-of-optical-remote-sensing-with-examples-from-landsat-8

[4] G. Vivone, R. Restaino, G. Licciardi, M. D. Mura, and J. Chanussot, "MultiResolution analysis and component substitution techniques for hyperspectral Pansharpening," in *Proc. Int. Geosci. Remote Sens. Symp.*, 2014, pp. 2649–2652.

[5] J. Qu, Y. Li, and W. Dong, "Guided filter and principal component analysis hybrid method for hyperspectral pansharpening," *J. Appl. Remote Sens.*, vol. 12, no. 1, 2018, Art. no. 015003.

[6] Y. Zhang, S. De Backer, and P. Scheunders, "Noise-resistant wavelet-based Bayesian fusion of multispectral and hyperspectral images," *IEEE Trans. Geosci. Remote Sens.*, vol. 47, no. 11, pp. 3834–3843, Nov. 2009.

[7] J. Bieniarz, D. Cerra, J. Avbelj, and P. Reinartz, "Hyperspectral image resolution enhancement based on spectral unmixing and information fusion," in *Proc. ISPRS Hann. Work. High-Resolution Earth Imag. Geospatial Inf.*, 2011, pp. 1–6.

[8] S. Chakravortty and P. Subramaniam, "Fusion of hyperspectral and multispectral image data for enhancement of spectral and spatial resolution," *Int. Arch. Photogramm. Remote Sens. Spat. Inf. Sci. - ISPRS Arch.*, vol. 40, no. 8, pp. 1099–1103, 2014.

[9] N. Yokoya, T. Yairi, and A. Iwasaki, "Coupled nonnegative matrix factorization unmixing for hyperspectral and multispectral data fusion," *IEEE Trans. Geosci. Remote Sens.*, vol. 50, no. 2, pp. 528–537, Feb. 2012.

[10] C. Lanaras, E. Baltsavias, and K. Schindler, "Hyperspectral superresolution by coupled spectral unmixing," in *Proc. IEEE Int. Conf. Comput. Vis.*, 2015, pp. 3586–3594.

[11] N. Akhtar, F. Shafait, and A. Mian, "Bayesian sparse representation for hyperspectral image super resolution," in *Proc. IEEE Comput. Soc. Conf. Comput. Vision Pattern Recognit.*, 2015, pp. 3631–3640.

[12] Z. H. Nezhad, A. Karami, R. Heylen, and P. Scheunders, "Fusion of Hyperspectral and multispectral images using spectral unmixing and sparse coding," *IEEE J. Sel. Top. Appl. Earth Obs. Remote Sens.*, vol. 9, no. 6, pp. 2377–2389, Jun. 2016.

[13] M. Simoes, J. Bioucas-Dias, L. B. Almeida, and J. Chanussot, "A convex formulation for hyperspectral image superresolution via subspace-based regularization," *IEEE Trans. Geosci. Remote Sens.*, vol. 53, no. 6, pp. 3373–3388, Jun. 2015.

[14] X. Luo, J. Yin, X. Luo, and X. Jia, "A novel adversarial based hyperspectral and multispectral image fusion," *Remote Sens.*, vol. 11, no. 5, 2019, Art. no. 492.

[15] C. Lanaras, E. Baltsavias, and K. Schindler, "Hyperspectral superresolution with spectral unmixing constraints," *Remote Sens.*, vol. 9, no. 11, 2017, Art. no. 1196.

[16] Q. Wei, J. Bioucas-Dias, N. Dobigeon, J.-Y. Tourneret, M. Chen, and S. Godsill, "Multi-band image fusion based on spectral unmixing," *IEEE Geosci. Remote Sens. Lett.*, vol. 54, no. 12, pp. 1–34, Dec. 2016.

[17] S. Li, R. Dian, L. Fang, and J. M. Bioucas-Dias, "Fusing Hyperspectral and multispectral images via coupled sparse tensor factorization," *IEEE Trans. Image Process.*, vol. 27, no. 8, pp. 4118–4130, Aug. 2018.

[18] W. Xie, J. Lei, Y. Cui, Y. Li, and Q. Du, "Hyperspectral pansharpening with deep priors," *IEEE Trans. Neural Netw. Learn. Syst.*, vol. 31, no. 5, pp. 1529–1543, May 2020.

[19] J. Bieniarz, D. Cerra, J. Avbelj, P. Reinartz, and R. Müller, "Hyperspectral image resolution enhancement based on spectral unmixing and information fusion," in *Proc. ISPRS - Int. Arch. Photogramm. Remote Sens. Spat. Inf. Sci.*, vol. XXXVIII-4/W19, 2011, pp. 33–37.

[20] C. Andreou and V. Karathanassi, "Estimation of the number of endmembers using robust outlier detection method," *IEEE J. Sel. Top. Appl. Earth Obs. Remote Sens.*, vol. 7, no. 1, pp. 247–256, Jan. 2014.

[21] M. E. Winter, "Fast autonomous spectral endmember determination in hyperspectral data," in *Proc. 13th Int. Conf. Appl. Geol. Remote Sens.*, 1999, pp. 337–344.

[22] Z. Zhu, S. Wang, and C. E. Woodcock, "Remote sensing of environment improvement and expansion of the Fmask algorithm : Cloud, cloud shadow, and snow detection for Landsats 4 − 7, 8, and Sentinel 2 images," *Remote Sens. Environ.*, vol. 159, pp. 269–277, 2015.

[23] W. Wanner, X. Li, and A. H. Strahler, "On the derivation of kernels for kernel-driven models of bidirectional reflectance," *J. Geophys. Res.*, vol. 100, no. D10, 1995, Art. no. 21077.

[24] J.-L. Roujean, M. Leroy, and P.-Y. Deschamps, "A bidirectional reflectance model of the Earth's surface for the correction of remote sensing data," *J. Geophys. Res.*, vol. 97, no. D18, 1992, Art. no. 20455.

[25] K. Kotwal and S. Chaudhuri, "A novel approach to quantitative evaluation of hyperspectral image fusion techniques," *Inf. Fusion*, vol. 14, no 1, pp. 5–18, 2013.

[26] J. E. O'Reilly and P. J. Werdell, "Chlorophyll algorithms for ocean color sensors - OC4, OC5 & OC6," *Remote Sens. Environ.*, vol. 229, pp. 32–47, 2019.

[27] A. L. Delgado *et al.*, "Evaluation of derived total suspended matter products from ocean and land colour instrument imagery (OLCI) in the inner and mid-shelf of Buenos Aires Province (Argentina)," *Earth Sp. Sci. Open Arch.*, 2018, doi: 10.1002/essoar.10500050.1.

[28] H. Liu, Q. Li, T. Shi, S. Hu, G. Wu, and Q. Zhou, "Application of Sentinel 2 MSI images to retrieve suspended particulate matter concentrations in Poyang lake," *Remote Sens.*, vol. 9, no. 7, 2017, Art. no. 761.

[29] B. Nechad, K. G. Ruddick, and Y. Park, "Calibration and validation of a generic multisensor algorithm for mapping of total suspended matter in turbid waters," *Remote Sens. Environ.*, vol. 14, no. 4, pp. 854–866, 2010.

Maria Kremezi received the M.Sc. degree in surveying engineering from National Technical University of Athens, NTUA, Athens, Greece, in 2016. She is currently working toward the Ph.D. degree in remote sensing at NTUA, Athens, Greece.

She has three years' experience as a Researcher with the Remote Sensing Laboratory, NTUA. During her Ph.D. studies, her research interests focus on hyperspectral remote sensing with emphasis on image fusion theory and techniques and the exploitation of spectral unmixing capabilities for hyperspectral image fusion. She is the author of publications in International Scientific Journals and Proceedings of International Conferences.

Vassilia Karathanassi received the B.S. degree in rural and surveying engineering from National Technical University of Athens, NTUA, Athens, Greece, the M.S. degree in urban planning-geography from Paris V and the Ph.D. degree in remote sensing from NTUA.

Since 2000, she has been a Professor with the School of the Rural and Surveying Engineering, specialized on hyperspectral/multispectral remote sensing and InSAR, DInSAR processing and applications. She teaches multiple undergraduate and postgraduate courses. She has supervised more than 35 undergraduate, 5 master's theses, 8 Ph.D. theses (4 of them completed), and 1 postdoctoral research. Her published research work includes more than 95 papers and 1 chapter in the book Hyperspectral Remote Sensing. Furthermore, she is involved in EU and national excellence/competitive research projects as a coordinator, as a Principal Investigator and as a Researcher toward the design, development and validation of state-of-the-art methodologies and cutting-edge technology in Remote Sensing and Earth Observation.